HAL
open science

Rise and fall, and slow rise again, of operator entanglement under dephasing

David Wellnitz, Guillermo Preisser, Vincenzo Alba, Jerome Dubail, Johannes Schachenmayer

To cite this version:

David Wellnitz, Guillermo Preisser, Vincenzo Alba, Jerome Dubail, Johannes Schachenmayer. Rise and fall, and slow rise again, of operator entanglement under dephasing. Physical Review Letters, 2022, 129 (17), pp.170401. 10.1103/PhysRevLett.129.170401 . hal-03546884

HAL Id: hal-03546884

https://hal.science/hal-03546884v1

Submitted on 24 Apr 2023

HAL is a multi-disciplinary open access archive for the deposit and dissemination of scientific research documents, whether they are published or not. The documents may come from teaching and research institutions in France or abroad, or from public or private research centers.

L'archive ouverte pluridisciplinaire **HAL**, est destinée au dépôt et à la diffusion de documents scientifiques de niveau recherche, publiés ou non, émanant des établissements d'enseignement et de recherche français ou étrangers, des laboratoires publics ou privés.

Rise and fall, and slow rise again, of operator entanglement under dephasing

D. Wellnitz,[1,2] G. Preisser,[1] V. Alba,[3] J. Dubail,[4,1] and J. Schachenmayer[1,2,*]

[1] *ISIS (UMR 7006) and CESQ, CNRS and Université de Strasbourg, 67000 Strasbourg, France*
[2] *IPCMS (UMR 7504), CNRS, 67000 Strasbourg, France*
[3] *Dipartimento di Fisica, Università di Pisa, and INFN Sezione di Pisa, Largo Bruno Pontecorvo 3, Pisa, Italy*
[4] *Université de Lorraine, CNRS, LPCT, F-54000 Nancy, France*

(Dated: October 24, 2022)

The operator space entanglement entropy, or simply 'operator entanglement' (OE), is an indicator of the complexity of quantum operators and of their approximability by Matrix Product Operators (MPO). We study the OE of the density matrix of 1D many-body models undergoing dissipative evolution. It is expected that, after an initial linear growth reminiscent of unitary quench dynamics, the OE should be suppressed by dissipative processes as the system evolves to a simple stationary state. Surprisingly, we find that this scenario breaks down for one of the most fundamental dissipative mechanisms: dephasing. Under dephasing, after the initial 'rise and fall' the OE can rise again, increasing logarithmically at long times. Using a combination of MPO simulations for chains of infinite length and analytical arguments valid for strong dephasing, we demonstrate that this growth is inherent to a $U(1)$ conservation law. We argue that in an XXZ spin-model and a Bose-Hubbard model the OE grows universally as $\frac{1}{4}\log_2 t$ at long times, and as $\frac{1}{2}\log_2 t$ for a Fermi-Hubbard model. We trace this behavior back to anomalous classical diffusion processes.

arXiv:2201.05099v2 [quant-ph] 21 Oct 2022

The study of quantum many-body systems through the prism of their quantum entanglement continues to prove extremely fruitful [1, 2]. In particular, the growth of entanglement in time-evolving quantum many-body systems is of fundamental interest [3–8]: not only is it useful to characterize the dynamics, but the amount of entanglement also indicates whether a quantum evolution can be efficiently simulated on a classical computer. In one dimension (1D) the connection can be made via the concept of matrix product states (MPS) [9–12]. An MPS is a decomposition of a many-body state vector into a product of $\chi \times \chi$ matrices (where the entries of the matrices are local kets). In such a representation, the bipartite von Neumann entanglement entropy S is bounded by $\max[S] = \log_2(\chi)$. Consequently, to represent a physical state $|\psi(t)\rangle$ with entanglement entropy $S(t)$ as an MPS, the matrix size (or 'bond dimension') has to grow at least as $\chi \propto 2^{S(t)}$ with time. For example, an evolution where S increases linear in time can therefore be considered computationally hard [13].

The past few years have seen the arrival of novel experiments capable of synthetically engineering quantum many-body models in controllable and clean environments, e.g. using optically trapped ultracold atoms [14–17], molecules [18], or ions [19]. Since such experiments are currently bringing the goal of analog quantum simulation into sight [20, 21], the question of entanglement growth, and thus classical simulability, has become very important.

Every experiment has small couplings to its environment, and should therefore be considered as an open quantum system described by a density matrix $\hat{\rho}$. Analogously to MPSs for pure states, also a matrix product operator (MPO) form of the density matrix $\hat{\rho}$ can be defined. An MPO form allows to easily express the density matrix as Schmidt decomposition between a left and a right block:

$$\hat{\rho} = \sum_a \lambda_a \hat{\tau}_a^{[L]} \hat{\tau}_a^{[R]}, \tag{1}$$

with $\mathrm{Tr}(\hat{\tau}_a^{[L/R]} \hat{\tau}_b^{[L/R]}) = \delta_{ab}$, and λ_a the Schmidt coefficients [schematically this is depicted in Fig. 1(b)]. The bipartite entropy of this decomposition is given by the 'operator space entanglement entropy' or simply 'operator entanglement' (OE) defined as [7, 22–30]

$$S_{\mathrm{OP}} = -\sum_a \lambda_a^2 \log_2\left(\lambda_a^2\right). \tag{2}$$

The OE quantifies how many Schmidt values are at least needed for faithfully approximating decomposition (1), and thus indicates the efficiency of an MPO representation [31]. It can be easily computed numerically [25, 27, 28, 32, 33] and is amenable to analytical treatment [26, 34, 35]. We stress that OE is not necessarily connected to genuine quantum entanglement between distinct blocks of spins when $\hat{\rho}$ is a mixed state. Still, it is a crucial quantity as it puts severe restrictions on the possibility to approximate $\hat{\rho}$ by an MPO. Furthermore, OE can give insights into quantum many body effects such as quantum chaos and information scrambling [27, 29, 30].

Here, we analyze the far-from-equilibrium dynamics of the OE, S_{OP}, in open many-body quantum systems. Our models include coherent nearest-neighbor Hamiltonian couplings that compete with incoherent single-particle dephasing [36–40] at rate γ [see sketch in Fig. 1(a)]. Under dephasing, fluctuations and coherences can decay towards equilibrium in a universal algebraic and subdiffusive manor [41–44]. We treat dissipation in a Lindblad master equation. Dephasing arises due to a coupling with the environment in which local magnetization

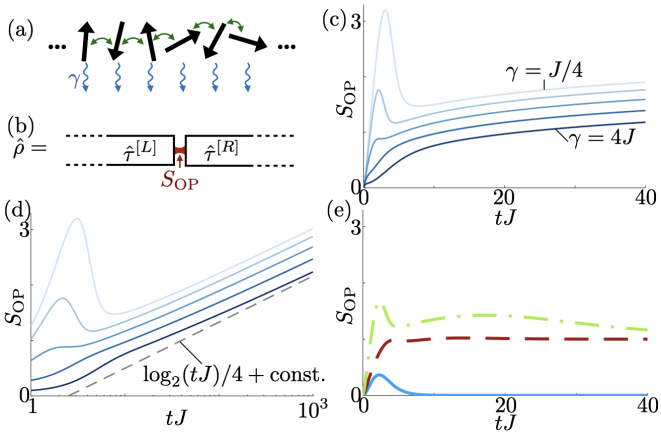

FIG. 1. (a) We compute dynamics of spin chains with coherent nearest-neighbor couplings (double-arrows) and local dephasing at rate γ (wiggly arrows). (b) We analyze the growth of OE ($S_{\rm OP}$) for a bipartition of an infinite chain into a left/right block [from a Schmidt decomposition of the density matrix $\hat{\rho}$, see Eq. (1)]. (c) Time evolution of $S_{\rm OP}$ for a Néel state in the XXZ model for different values of $\gamma = J/4, J/2, J, 2J, 4J$ in order of increasing darkness (anisotropy $J_z = -J$). (d) Same as (c), demonstrating logarithmic growth at long times (log-scale time axis). Grey dashed: Analytic long-time prediction: $S_{\rm OP} = \log_2(Jt)/4 + \text{const.}$ (e) $S_{\rm OP}$ for dynamics in models breaking magnetization conservation. Green dash-dotted: XYZ model ($J_x = J, J_y = 0.8J, J_z = -J/2, \gamma = J/2$), Red dashed: transverse field Ising model ($h_z = J, \gamma = J/2$), blue solid: XXZ model with initial Néel state in x-direction ($J_z = -J/2, \gamma = J/2$). Results converged for time step $\Delta tJ = 0.2$ [$\Delta tJ = 0.5$ for panel (d) at long times] and different values for the bond dimension $\chi = 256, 512, 1024$ (see Appendix for convergence).

is preserved, e.g. for laser driven transitions due to laser-phase fluctuations [45, 46], or due to spontaneous photo-absorption of lattice photons in optical lattices [47]. We compute the evolution of $S_{\rm OP}$ for an infinite MPO representation of the full density matrix using an infinite time evolving block decimation algorithm (iTEBD) with re-orthogonalization [48].

Surprisingly, we find that for the magnetization conserving XXZ model and well-defined initial magnetization [see text below Eq. (3) for the definition of our models], the OE exhibits a universal logarithmic growth at long times [see Fig. 1(c/d)]. An identical universal behavior is also observed for particle number conserving Bose- and Fermi-Hubbard models [see discussion below]. Strikingly, as shown in Fig. 1(e), this logarithmic growth breaks down if the symmetry is broken by initial states, or for Liouvillians without magnetization conservation (see Appendix for more examples). In the latter scenarios $S_{\rm OP}$ saturates, or even vanishes at long times. In this paper we explain this behavior by considering symmetry-resolved OE in combination with known results for classical models of interacting particles [49–51].

Model — We focus on infinite spin-1/2 chains, which evolve under the general Hamiltonian ($\hbar \equiv 1$):

$$\hat{H} = \frac{1}{4}\sum_i \left(J_x \hat{\sigma}_i^x \hat{\sigma}_{i+1}^x + J_y \hat{\sigma}_i^y \hat{\sigma}_{i+1}^y + J_z \hat{\sigma}_i^z \hat{\sigma}_{i+1}^z\right) + \frac{h_z}{2}\sum_i \hat{\sigma}_i^z . \tag{3}$$

Here, $\hat{\sigma}_i^{x,y,z}$ denote standard Pauli matrices defined in a local basis $|\downarrow,\uparrow\rangle_i$, $J_{x,y,z}$ are the respective nearest-neighbor spin couplings, and h_z is a field strength along the z direction. Our Hamiltonian (3) includes: i) the *XXZ model*, with $J_x = J_y \equiv J$, $h_z = 0$; ii) an *XYZ model*, with $J_x \equiv J$, $J_x \neq J_y$, $h_z = 0$; and iii) a *transverse Ising model*, with $J_x \equiv J$, $J_y = J_z = 0$, $h_z \neq 0$. We are interested in the dynamics of highly-excited states. Here, we choose pure Néel product states polarized along the z direction, $\hat{\rho}_0 = |\psi_0\rangle\langle\psi_0|$ with $|\psi_0\rangle = \bigotimes_i |\uparrow\rangle_{2i-1}|\downarrow\rangle_{2i}$, or a tilted Néel state along the x direction, $|\psi_0\rangle = \bigotimes_i |\rightarrow\rangle_{2i-1}|\leftarrow\rangle_{2i}$ with $|\leftrightarrows\rangle_i = (|\uparrow\rangle_i \mp |\downarrow\rangle_i)/\sqrt{2}$. Dynamics is governed by a Lindblad master equation,

$$\frac{d}{dt}\hat{\rho} = -\mathrm{i}[\hat{H},\hat{\rho}] + \sum_i \mathcal{D}^{[i]}\hat{\rho} \equiv \mathcal{L}\hat{\rho}\,, \tag{4}$$

with the local dephasing super-operators $\mathcal{D}^{[i]}\hat{\rho} = \gamma/2(\hat{\sigma}_i^z\hat{\rho}\hat{\sigma}_i^z - \hat{\rho})$ and the Liouvillian super-operator $\mathcal{L}$.

MPO decomposition and OE — For L spins, the full many-body density matrix $\hat{\rho}$ of a spin-1/2 system is a $2^L \times 2^L$ hermitian matrix with unit trace. The amount of information encoded in $\hat{\rho}$ can be effectively compressed using matrix product decompositions [11, 12]. This can be done in different ways [52]: For instance, by decomposing $\hat{\rho}$ into a particular (not unique) statistical mixture of pure states, while using an MPS for the latter. Then, the Lindblad dynamics can be computed using quantum trajectories [53]. Alternatively, one can use a direct MPO representation for $\hat{\rho}$, e.g. simply by effectively vectorizing local density matrices [54], or by constructing MPOs in a locally purified form which preserves positivity [55, 56].

Here, we decompose $\hat{\rho}$ into a canonical MPO form [54], which is formally achieved by an iterative application of the Schmidt decomposition from Eq. (1), until each spin n is described by a matrix of unique local operators $\hat{\gamma}^{[n]}_{a_n,a_{n+1}}$, i.e. $\hat{\rho} = \sum_{\{a_n\}}\prod_n \lambda_{a_n}\hat{\gamma}^{[n]}_{a_n,a_{n+1}}$. By choosing local basis operators, $\hat{e}_{i_n}$, for the density matrix of spin n, we can then decompose:

$$\hat{\rho} = \sum_{\{i_n\}}\sum_{\{a_n\}}^{\chi}\prod_n \Gamma^{[n]\,i_n}_{a_n a_{n+1}}\lambda^{[n]}_{a_n}\bigotimes_n \hat{e}_{i_n}\,, \tag{5}$$

where $\Gamma^{[n]}$ are three-dimensional tensors and $\lambda^{[n]}$ the Schmidt vectors. Tensors are truncated at a maximum MPO bond dimension χ. All results shown are numerically converged in χ (see Appendix). For $\hat{e}_i$ we choose local eigenoperators for the multiplication with $\hat{\sigma}^z$ from

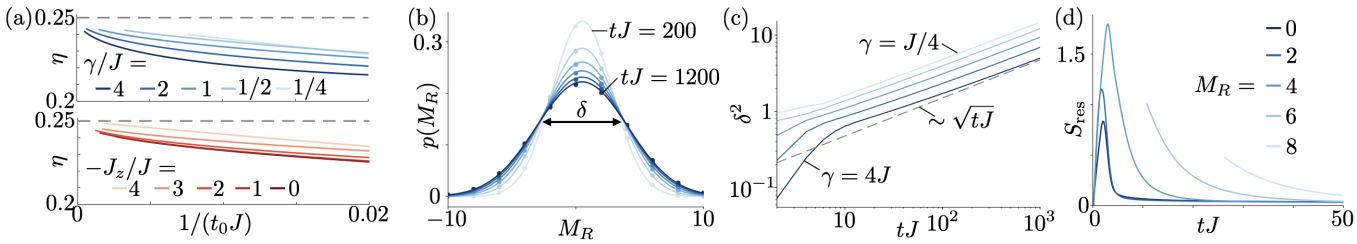

FIG. 2. (a) Numerical determination of η for long times. η at time $t_0 J$ is obtained as the local tangent to $S_{\rm OP}(t) = S_0 + \eta \log(tJ)$ at $t_0 J$. We find $\eta \to 1/4$ (grey dashed line) for all parameters and $t_0 \to \infty$. Top (blue): Fixed $J_z = -J$ and various $\gamma/J = 1/4, 1/2, 1, 2, 4$. Bottom (red): Fixed $\gamma = J$ and various $-J_z/J = 0, 1, 2, 3, 4$. (b) Probabilities $p(M_R)$ for right-half magnetization M_R of the infinite chain (see text) at increasingly late times ($200 \leq tJ \leq 1200$ from light to dark, $J_z = -J$, $\gamma = J/2$. Lines are Gaussian fits. (c) Variance δ^2 of Gaussian fits [as in (b)] as a function of time for $J_z = -J$ and $\gamma/J = 1/4, 1/2, 1, 2, 4$ (light to dark). The grey dashed line indicates $\delta^2 \sim \sqrt{tJ}$ (double-log scale). (d) Symmetry-resolved operator entanglement entropies $S_{\rm res}$ as a function of time (see text). For short times and the larger $M_R = 6, 8$ the probabilities $p(M_R)$ are exponentially suppressed and no sub-machine-precision data could be extracted. Same parameters as panel (b). Results converged for $\Delta t J = 0.5$ [(a)-(c)] and $\Delta t J = 0.1$ [(d)] and different values of $\chi = 512, 1024, 2048$ (see Appendix).

the left and right, to take advantage of the magnetization conservation (see below). Both the initial state and the Hamiltonian are invariant under translation by two lattice sites. As a consequence, in Eq. (5) one has $\Gamma^{[n+2]} = \Gamma^{[n]}$ and $\lambda^{[n+2]} = \lambda^{[n]}$ [48, 57], and only two Γ and λ tensors are needed to encode a density matrix. The time evolution is then computed with a fourth order Trotter decomposition of the matrix exponential of the Liouvillian $\exp(\mathcal{L}\Delta t)$ [48, 54, 58]. Importantly, since the dynamics is non-unitary, a naïve implementation of this algorithm destroys the orthogonality of the decomposition in Eq. (5), such that with time, the λs do not correspond to orthogonal Schmidt bases anymore. We fix this by re-orthogonalizing the tensors after updates [48].

When considering the XXZ model, the total magnetization $\hat{S}^z = \sum_n \hat{\sigma}^z_n$ is conserved. This means that $\hat{\rho}$ stays an eigenoperator of $\hat{S}^z$ in the sense that $\hat{S}^z \hat{\rho}(t) = M \hat{\rho}(t)$ at all times (for the Néel state, $M = 0$). Note that alternatively, one could also define a condition for multiplication from the right. Due to magnetization preservation, the $\hat{\tau}^{[R]}_a$ matrices in Eq. (1) can be chosen to be eigenoperators of the 'right-half magnetization' of the chain, $\hat{S}^z_R \equiv \sum_{n>0} \hat{\sigma}^z_n$ (w.l.o.g. we define the right half as $n > 0$), $\hat{S}^z_R \hat{\tau}^{[R]}_a = M_R \hat{\tau}^{[R]}_a$. Similarly, one can choose $\hat{\tau}^{[L]}_a$ to be eigenoperators of $\hat{S}^z_L \equiv \sum_{n \leq 0} \hat{\sigma}^z_n$ with $M_L = -M_R$. This means that the index a in Eq. (1) becomes a composite index $a \to (M_R, a')$, where a' distinguishes the Schmidt coefficients corresponding to the same M_R:

$$\hat{\rho} = \sum_{M_R} \sqrt{p_{M_R}} \sum_{a'} \widetilde{\lambda}_{M_R,a'} \hat{\tau}^{[L]}_{-M_R,a'} \hat{\tau}^{[R]}_{M_R,a'} \,. \tag{6}$$

Here we defined $\widetilde{\lambda}_{M_R,a} \equiv \lambda_{M_R,a}/\sqrt{p_{M_R}}$, with $p_{M_R} = \sum_a \lambda^2_{M_R,a}$ the probability of having magnetization M_R in the right half. The existence of the conservation law makes our simulations much more efficient, since the block-diagonal form of the tensors can be exploited.

Logarithmic increase of OE: Numerical results — In simulations in Fig. 1 we noticed a distinctive different behavior of OE growth at long times (log-growth) for the magnetization conserving XXZ model compared to other models breaking this conservation law. Quite generically, at times $t \ll \gamma^{-1}$, the dynamics is dominated by the Hamiltonian part in Eq. (4). Sufficiently pure states at such short times can be approximated by the state $|\psi_t\rangle = \mathrm{e}^{-\mathrm{i}\hat{H}t}|\psi_0\rangle$. In that case the OE is simply twice the entanglement entropy of $|\psi_t\rangle$ (see e.g. [26]), and it is well established that the latter generically grows linearly in time (in the absence of disorder). At times $t \gtrsim \gamma^{-1}$, the initial coherence is destroyed by dephasing, and the OE decreases (see Appendix for a more detailed discussion on the parameter dependence of the peak-heights). This 'rise and fall' is clearly visible in Fig. 1, and it is typical for OE dynamics, and also other quantities such as the mutual information [59, 60]. Typically, under the dynamics in Eq. (4) the system is expected to relax to a simple stationary state characterized by the conserved quantities of Eq. (4), or to the identity if there is no conservation law. The OE at late times converges towards the OE of that stationary state. This is visible in our simulations of the XYZ and Ising models, see Fig. 1(e). In this case only the parity $\hat{\Pi} = \bigotimes_i \hat{\sigma}^z_i$ is preserved by the dynamics. Since the initial Néel state is an eigenstate of $\hat{\Pi}$, the stationary density matrix is a projector on a fixed parity sector, $\frac{1}{2}(1 \pm \hat{\Pi})$, with the $\mathcal{O}(1)$ entropy $S_{\rm OP} = 1$ ($= \log_2 2$). For the XXZ chain with the initial tilted Néel along the x direction, even parity conservation is broken, and the stationary density matrix becomes the identity, $S_{\rm OP} = 0$. In stark contrast, for the XXZ chain and initial Néel state, after the rise and fall dynamics, the OE increases again at long times, see Fig. 1(c), and this second increase is logarithmic in time, see Fig. 1(d). More precisely, we find the long-time behavior $S_{\rm OP}(t \to \infty) = \eta \log_2(tJ) + S_0$, which we will also

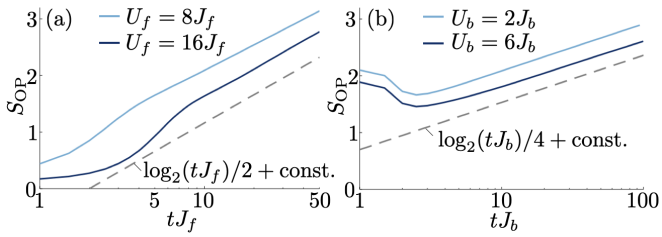

FIG. 3. Logarithmic OE growth in the Fermi-Hubbard (a) and Bose-Hubbard (b) models with dephasing for different interaction strengths $U_{f/b}$. The grey dashed lines indicate the analytically expected long-time growth (see Appendix). The initial states are: One fermion per site with alternating spins $|\cdots\uparrow\downarrow\uparrow\cdots\rangle$ (a) and alternating sites with 0 or 1 boson $|\cdots 101\cdots\rangle$ (b). Parameters: $\gamma_f = 8J_f$ (a) and $\gamma_b = 2J_b$ (b), $\chi = 512, 256$, $\Delta t J_{f/b} = 1/2$, maximum bosons per site $n_{\max} = 4$.

understand analytically below. The prefactor η converges universally to $\eta = 1/4$ independent on the precise values of γ and J_z, as shown in Fig. 2(a), and has also been observed with additional disorder [61]. The offset S_0 depends on the characteristic time-scale of the long-time diffusive dynamics set by J, J_z and γ (see Appendix). Note that we find the evolution of OE in the XXZ model to be independent of the signs of J and J_z.

Mechanism for logarithmic growth: Abelian symmetry and anomalous charge diffusion — To also analytically understand this behavior, we now consider the XXZ model evolution in the strong dephasing limit $\gamma \gg J$. The dissipators in the master equation (4) project the density matrix onto its diagonal part $\hat{\rho}_{\rm diag} = \sum_{\boldsymbol{\sigma}} \rho_{\boldsymbol{\sigma}\boldsymbol{\sigma}} |\boldsymbol{\sigma}\rangle\langle\boldsymbol{\sigma}|$, where the $\boldsymbol{\sigma}$ denote all binary vectors of spin-z configurations. The dynamics then reduces to a classical master equation for the probability $p_{\boldsymbol{\sigma}} = \rho_{\boldsymbol{\sigma}\boldsymbol{\sigma}}$, $dp_{\boldsymbol{\sigma}}/dt = \sum_{\boldsymbol{\sigma}'} \mathcal{M}_{\boldsymbol{\sigma}\boldsymbol{\sigma}'} p_{\boldsymbol{\sigma}'}$. The stochastic matrix $\mathcal{M}$ was determined in Ref. 37 in second-order perturbation theory starting from Eq. (4). It takes the form of an effective ferromagnetic Heisenberg Hamiltonian, $\mathcal{M} = -J^2/(8\gamma)\sum_i \left[\hat{\sigma}_i^x\hat{\sigma}_{i+1}^x + \hat{\sigma}_i^y\hat{\sigma}_{i+1}^y + \hat{\sigma}_i^z\hat{\sigma}_{i+1}^z - 1\right]$. Importantly, $\mathcal{M}$ is the stochastic matrix of the Symmetric Simple Exclusion Process (SEP) [62, 63], a model of classical hard-core particles that perform random walks.

Crucially, in the SEP, the mean squared displacement of a tagged particle grows as $\langle X_t^2\rangle \propto \sqrt{t}$ [50, 51, 64–67], as opposed to $\propto t$ for a usual random walk. This anomalous diffusion is universally found in problems of so-called 'single-file diffusion' [64, 68, 69], when classical particles diffuse in one-dimensional channels without bypassing each other. Here, it is now also tied to anomalous scaling of the particle number fluctuations between the left and right half-systems. If $\Delta N(t) = M_R(t)/2$ is the excess number of particles (w.r.t. the initial Néel state) in the right half-system at time t, and if we tag the particle initially at the origin, then one can estimate $\Delta N(t) \simeq \rho_0 X_t$, where $\rho_0 = 1/2$ is the particle density in the Néel state. Consequently, $\langle \Delta N(t)^2\rangle \simeq \rho_0^2\langle X_t^2\rangle \propto \sqrt{t}$. More generally, the probability distribution of $M_R(t)$ is found to obey a scaling form at long times [65]: $p(M_R(t) = m) \underset{t\to\infty}{\sim} \exp\left(\sqrt{t}\, G\left(\frac{m}{\sqrt{t}}\right)\right)$. Here, the large-deviation function G is non-positive, symmetric $[G(u) = G(-u)]$, diverges when $|u| \to \infty$, and has a single minimum at $u = 0$ (see [65]). In particular, away from the tails the distribution is Gaussian with standard deviation $\delta = t^{1/4}/\sqrt{|G''(0)|}$. The Shannon entropy associated to number fluctuations is then

$$\begin{aligned} S_{\rm num}(t) &= \sum_{m\in 2\mathbb{Z}} -p(m)\log_2 p(m) \\ &\simeq \int -\sqrt{\frac{2}{\pi\delta^2}}\mathrm{e}^{-\frac{m^2}{2\delta^2}} \log_2\left(\sqrt{\frac{2}{\pi\delta^2}}\mathrm{e}^{-\frac{m^2}{2\delta^2}}\right)\frac{dm}{2} \\ &= \log_2\delta + \log_2\left(\sqrt{\pi\mathrm{e}/2}\right) \underset{t\to\infty}{=} \frac{1}{4}\log_2 t + \mathcal{O}(1). \end{aligned} \tag{7}$$

It is no coincidence that $S_{\rm OP}$ grows in the same way as the number fluctuations $S_{\rm num}$ at long times (see below).

Away from the $\gamma/J \gg 1$ limit, the XXZ chain no longer reduces to the SEP. Nevertheless we find that the same type of anomalous scaling persists. This is confirmed in Fig. 2, where we show that, for times accessible numerically, $p(M_R = m)$ is approximately Gaussian [Fig. 2(b)] with width $\delta \propto t^{\frac{1}{4}}$ [Fig. 2(c)]. Thus, even though the exact correspondence with the SEP breaks down at finite γ/J, the scaling of $S_{\rm num}$ in Eq. (7) remains unchanged. This result is also consistent with previous studies of transport in the XXZ and related models [70–73].

Symmetry-resolved OE — We now show how the relation between $S_{\rm OP}$ and $S_{\rm num}$ can be revealed in so-called symmetry resolved operator entanglement. From Eq. (6) we can derive a decomposition of the OE into the form:

$$S_{\rm OP} = \sum_{M_R} p_{M_R} S_{\rm res}(M_R) + S_{\rm num}(p_{M_R}), \tag{8}$$

where the 'symmetry-resolved entanglement entropies' are $S_{\rm res}(M_R) = -\sum_a \widetilde{\lambda}^2_{M_R,a}\log_2(\widetilde{\lambda}^2_{M_R,a})$, and $S_{\rm num}$ is given in Eq. (7). Such symmetry-resolved entropies have attracted attention recently [8, 74–78]. In Fig. 2(d) we display $S_{\rm res}(M_R)$ for different values of M_R. Also $S_{\rm res}$ exhibits the 'rise and fall' phenomenon discussed above, but independent of M_R they decrease to very small values at late times. This means that the logarithmic increase $S_{\rm OP}$ is solely due to the growth of $S_{\rm num}$.

Fermi- and Bose-Hubbard model — To demonstrate the generality of the logarithmic OE growth, we discuss two additional paradigmatic many-body setups featuring number conservation: i) a Fermi-Hubbard (FH) model, $\hat{H}_{\rm FH} = -J_f\sum_{n,\sigma}(\hat{c}^\dagger_{\sigma,n}\hat{c}_{\sigma,n+1} + \text{h.c.}) +$

$U_f \sum_n \hat{c}^\dagger_{\uparrow,n}\hat{c}^\dagger_{\downarrow,n}\hat{c}_{\uparrow,n}\hat{c}_{\downarrow,n}$ with creation operators for spinfull fermions on site n, $\hat{c}^\dagger_{\sigma,n}$ ($\sigma = \uparrow,\downarrow$); and ii) a Bose-Hubbard (BH) model, $\hat{H}_{\rm BH} = -J_b \sum_n (\hat{b}^\dagger_n \hat{b}_{n+1} + \text{h.c.}) + U_b/2 \sum_n \hat{b}^\dagger_n \hat{b}^\dagger_n \hat{b}_n \hat{b}_n$, for bosons created by $\hat{b}^\dagger_n$. In both cases we consider dephasing $\mathcal{D}^{[k]}\hat{\rho} = \gamma \hat{L}_k \rho \hat{L}^\dagger_k - \gamma(\hat{L}^\dagger_k \hat{L}_k \hat{\rho} + \hat{\rho}\hat{L}^\dagger_k \hat{L}_k)/2$, where $\hat{L}_{\sigma,n} = \hat{c}^\dagger_{\sigma,n}\hat{c}_{\sigma,n}$ and $\hat{L}_n = \hat{b}^\dagger_n \hat{b}_n$ in the FH and BH case, respectively. As demonstrated in Fig. 3, both models also exhibit a long-time logarithmic OE growth. In the FH model, we observe $S_{\rm OP} \sim \log_2(tJ_f)/2$. For $\gamma \gg J_f, U_f$, this can be understood analytically by considering the FH chain as the sum of two chains, one for each spin degree of freedom, both of which are described by the SEP and exhibit $S_{\rm OP} \sim \log_2(tJ_f)/4$. Here, interactions contribute only at higher orders (see Appendix). The BH model exhibits $S_{\rm OP} \sim \log_2(tJ_b)/4$ analogous to the XXZ model. For large $U_b \gg \gamma \gg J_b$ the creation of doublons is energetically suppressed, leading back to the SEP. For finite interaction strength ($\gamma \gg J_b, U_b$), a different classical limit is reached, which also features logarithmic OE growth with a prefactor close to 1/4 stemming from a 'Symmetric Inclusion Process' (see Appendix and Ref. [63]).

Conclusion — We showed that in a dissipative system possessing a $U(1)$ conservation law the operator entanglement grows logarithmically at long times. We pinpointed the mechanism that leads to this logarithmic growth, and identified its prefactor with the [possibly anomalous] exponent characterizing the fluctuations of the charge associated with the $U(1)$ symmetry. Our results and methods are of general interest to studies of imperfect quantum computation and quantum simulation platforms, currently pushing into a regime where they may offer a quantum advantage. The entanglement entropy dynamics we study here connects directly to similar results obtained for discrete quantum circuit models [27, 32, 79, 80], or to other dissipative simulation methods such as quantum trajectories [81, 82]. An understanding of the destructive processes of the environment on dynamics are essential, and the interplay between dissipation and coherent couplings can lead to interesting physics or state engineering (e.g. [83–86]). In the future, it will be interesting to investigate how the presence of more complex symmetries such as SU(N) impacts entanglement dynamics.

Acknowledgments We thank P. Calabrese, O. Castro-Alvaredo, A. Grabsch, G. Misguich, S. Murciano, G. Pupillo and G. Schütz for helpful discussions. This work was supported by LabEx NIE under contract ANR-11-LABX0058 NIE, and the QUSTEC program, which has received funding from the European Union's Horizon 2020 research and innovation program under the Marie Skłodowska-Curie grant agreement number 847471. This work is part of the Interdisciplinary Thematic Institute QMat, as part of the ITI 2021-2028 program of the University of Strasbourg, CNRS and Inserm, and was supported by IdEx Unistra (ANR-10-IDEX-0002), SFRI STRAT'US project (ANR-20-SFRI-0012), and EUR QMAT ANR-17-EURE-0024 under the framework of the French Investments for the Future Program. Our MPO codes make use of the intelligent tensor library (ITensor) [87]. Computations were carried out using resources of the High Performance Computing Center of the University of Strasbourg, funded by Equip@Meso (as part of the Investments for the Future Program) and CPER Alsacalcul/Big Data.

APPENDICES

In Sec. A, we provide details on the numerical convergence. In Sec. B, we discuss a breaking of magnetization conservation on different levels. In Sec. C we show numerical results on the parameter dependence of the short time peaks of the OE. In Sec. D, we discuss the perturbative estimate for the offset of the operator entanglement. In Sec. E, we identify the strong dephasing limits of the Fermi-Hubbard model, and of the Bose-Hubbard model, which are instrumental for explaining the prefactors of the logarithmic growth of the OE observed in the main text.

Appendix A: Details on numerical convergence

For solving the time-evolution with the iTEBD algorithm [48, 57] we make use of a Trotter decomposition of the matrix exponential of the super-operator governing the full dissipative dynamics [54]. In order to reach long time-scales, we implement 4-th order decomposition [58], which allowed for time-step converged results even up to step sizes of $\Delta t = 1/(2J)$ [see Fig. S1(a)]. Δt signifies the full time step, which is composed of individual gates with time-steps of length $\Delta t/12$ and $\Delta t/6$. In particular, we use the method

$$(1)^T(1)(1)^T(-2)(1)^T(1)^T(1)^T(1)^T(1)(1)^T(1)(1)(1)(1)(-2)^T(1)(1)^T(1)\,. \tag{S1}$$

Throughout the paper we only show simulations up to times until which the results are converged in the MPO bond dimension χ, defined in the truncated MPO decomposition in Eq. (5). In practice, we ran simulations repeatedly, doubling bond dimensions in the different runs until lines become visually indistinguishable. We varied the bond dimension in the range $\chi = 128, 256, 512, 1024, 2048$. Note that e.g. for $\chi = 1024$, a maximum possible entropy of $S_{\mathrm{OP}} \leq \log_2(\chi) = 10$ is theoretically supported. Naturally, the evolution producing the largest OE required the largest values of χ. The convergence plots in Fig. S1(b) and Fig. S1(c) demonstrate this procedure for "worst-case" scenarios (i.e. the data with the largest OE values and for long times). We choose the data from Fig. 1(d) with $\gamma = J/4$, simulated up to long times, and the data for Fig. 3(a) with $J_z/J = -1$ and $\gamma = J/8$, which reached the largest values in the short time peak $S_{\mathrm{OP}} \sim 6$.

In particular, the following parameters have been used for the figures in the main text:

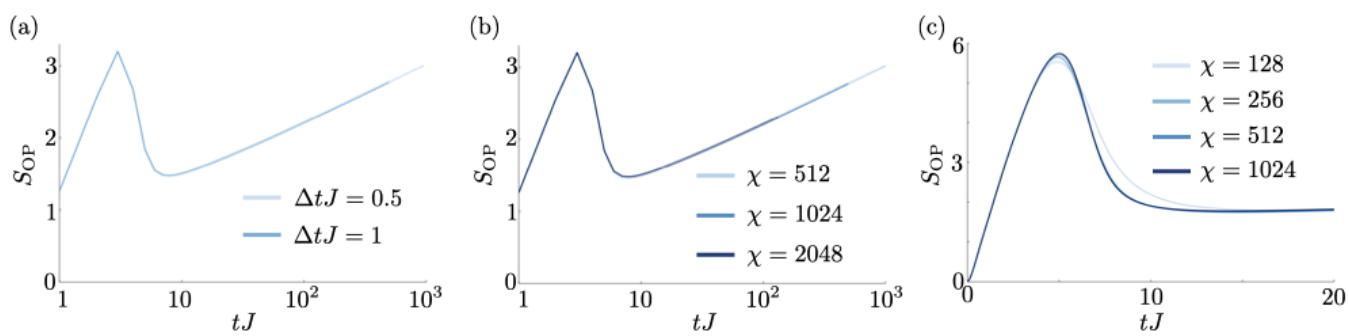

FIG. S1. (a) Convergence in the time-step Δt (in units $1/J$) for $\gamma = J/4$, $J_z = -J$, $\chi = 1024$. (b) Convergence in χ for $\gamma = J/4$, $J_z = -J$, $\Delta tJ = 0.5$. (c) Convergence in χ for $\gamma = J/8$, $J_z = -J$, $\Delta tJ = 0.1$

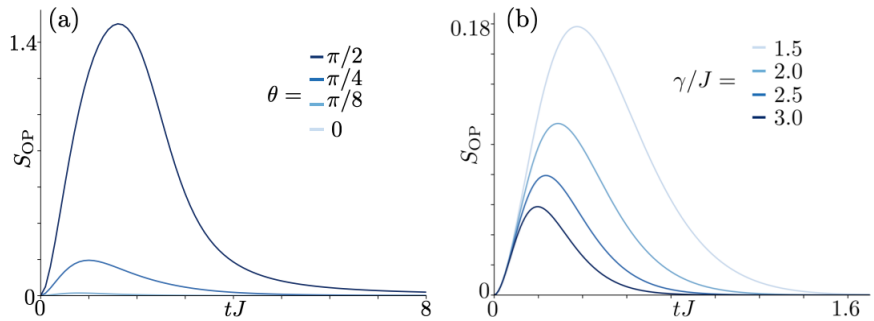

FIG. S2. Rise and fall of operator entanglement without magnetization conservation. (a) We consider the XXZ model with dephasing, as in the main text, for $J_z = -J$, $\gamma = J/2$. The initial state is a fully polarized state $\bigotimes_n \exp[\mathrm{i}\theta\hat{\sigma}_n^{(x)}]\,|{\downarrow}\rangle_n$, which are not and eigenstate of $\hat{S}_z$ (except for $\theta = 0$). (b) We consider the XXZ model with $J_z = -J$ for a Néel initial state as in the main text. Instead of dephasing, we consider non-conserving dissipation $\mathcal{D}_n^{\pm}\hat{\rho} = \gamma/2(2\hat{\sigma}_n^{\pm}\hat{\rho}\sigma_n^{\mp} - \hat{\sigma}_n^{\mp}\hat{\sigma}_n^{\pm}\hat{\rho} - \hat{\rho}\hat{\sigma}_n^{\mp}\hat{\sigma}_n^{\pm})$, and for various rates γ. Simulations for $\chi = 128$, $\Delta t J = 0.1$

Figure	$-J_z/J$	γ/J	χ	$\Delta t J$
Fig. 1(c)	1	0.25	512	0.2
Fig. 1(c)	1	≥ 0.5	256	0.1/0.2
Fig. 1(d)(short times)	1	≤ 1	1024	0.1/0.2
Fig. 1(d)(short times)	1	> 1	256	0.1/0.2
Fig. 1(d)(long times)	1	all	512	0.5
Fig. 1(e)	all	all	256	0.2
Fig. 2(a)/S3(b)	1	0.25	2048	0.5
Fig. 2(a)/S3(b)	1	0.5, 1	1024	0.5
Fig. 2(a)/S3(b)	1	2, 4	512	0.5
Fig. 2(a)/S3(b)	all	1	1024	0.5
Fig. 2(b)	1	0.5	512	0.5
Fig. 2(c)	1	all	512	0.5
Fig. 2(d)	1	0.5	1024	0.1
Fig. 3(a)	all	—	512	0.5
Fig. 3(b)	all	—	256	0.5
Fig. S3(a)	all	0.125	1024	0.1
Fig. S3(a)	all	≥ 0.25	512	0.1/0.2

Whenever two Δt values are given, different Δts were used for different parameters for historic reasons, but are clearly converged in either case.

Appendix B: Breaking magnetization conservation

In this section, we give a few more examples without magnetization conservation. First, we discuss fully polarized states that are tilted at an angle θ, $\bigotimes_n \exp[\mathrm{i}\theta\hat{\sigma}_n^{(x)}]\,|{\downarrow}\rangle_n$. For $0 < \theta < \pi$, these states are not eigenstates of $\hat{S}_z$. We find that after the initial growth, the OE decays to zero, just like for the initial tilted Néel state. For the special cases $\theta = 0(\pi)$, the state $|\cdots{\downarrow}{\downarrow}{\downarrow}{\downarrow}\cdots\rangle$ ($|\cdots{\uparrow}{\uparrow}{\uparrow}{\uparrow}\cdots\rangle$) is an eigenstate of the Liouvillian, and thus the OE remains zero at all times.

If magnetization conservation is broken on the level of the Liouvillian, we find a similar rise and fall of OE, which remains zero at long times [see Fig. S2(b)]. For the case of both an incoherent pump and and decay at rate γ, after the initial rise and fall, we expect the steady state to be the (trivial) infinite temperature state with $S_{\rm OP} = 0$.

Appendix C: Short-time peak heights

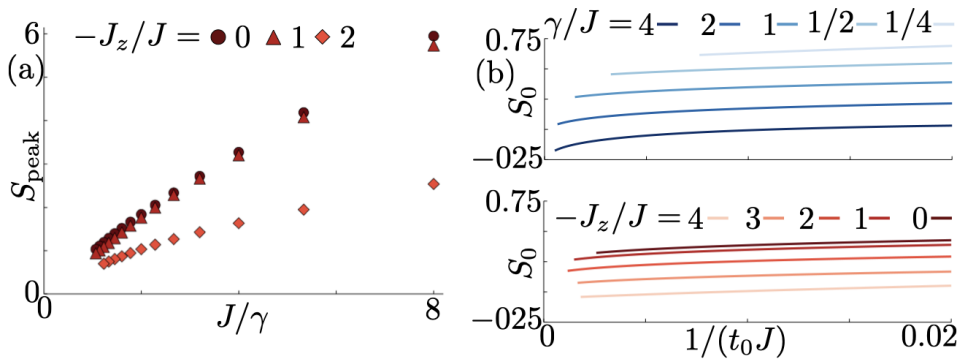

FIG. S3. (a) Short-time peak-height of S_{OP} as a function of $1/\gamma$ for different J_z. (b) Offset S_0 (extracted from fits as in Fig. 2 in the main manuscript) as a function of the inverse tangent time $1/(t_0 J)$. Blue lines (top) indicate variable γ at fixed $J_z = -J$, red lines (bottom) indicate variable J_z at fixed γ. Results converged for (a) $\Delta t J = 0.1$ and (b) $\Delta t J = 0.5$, and different values of $\chi = 512, 1024, 2048$

Whether a state can be efficiently approximated by an MPO is determined by the OE of that state, which has a local maximum at short times. Thus, until not too long times, the approximability of the dynamics is determined by the value at this maximum S_{peak}. This value is shown in Fig. S3(a) as a function of the dephasing rate γ and the interaction strength J_z. We find that generally the peak-height grows as $S_{\text{peak}} \sim 1/\gamma$ for small γ. Interestingly, S_{peak} decreases when increasing the spin interaction strength $|J_z|$. As a consequence, the dynamics under strong dephasing can always be simulated, while for small dephasing the dynamics can only be simulated in the presence of strong interactions (large $|J_z|$).

Appendix D: OE offset scaling

Whether a state can be efficiently approximated by an MPO is determined by the OE of that state, which is at long times dominated by the logarithmic growth $S_{\text{OP}} = \log_2(tJ)/4 + S_0$. Since logarithmic growth is very slow, the offset is also important. We find that the offset S_0 decreases with increasing $|J_z|$ or γ [see Fig. S3(b)] when extrapolating to $t_0 \to \infty$. The approximately equal spacing of lines in a regime of large γ (when doubling γ) indicates a scaling of $S_0 \sim \log_2(1/\gamma)$ in this regime. This is confirmed by the perturbative argument given below, which leads to $S_0 = \log_2(J/2\sqrt{4\gamma^2 + J_z^2})/4 + \mathcal{O}(1)$.

In the analytical model, the offsets are given by the time scale of the transfer, as the multiplicative transfer rate under the logarithm becomes an additive constant (see below). Cai and Barthel have computed the transfer rates perturbatively for small $J \ll \gamma$, as discussed in the following [37].

We start by writing the evolution operator as a sum $\mathcal{L} = \mathcal{L}_0 + \mathcal{L}_1$ with $\mathcal{L}_0 = -\mathrm{i}[\hat{H}_0, \cdot] + \sum_i \mathcal{L}^{[i]}$ and $\mathcal{L}_1 = -\mathrm{i}[\hat{H}_1, \cdot]$. Here, the Hamiltonian is separated into interaction $\hat{H}_0 = J_z/4 \sum_i \hat{\sigma}_i^z \hat{\sigma}_{i+1}^z$ and $\hat{H}_1 = J/2 \sum_i \left(\hat{\sigma}_i^+ \hat{\sigma}_{i+1}^- + \hat{\sigma}_i^- \hat{\sigma}_{i+1}^+\right)$. In the limit of strong dissipation, we can then consider perturbation theory for small $\mathcal{L}_1$.

The eigenstates of $\mathcal{L}_0$ are product states in the z eigenbasis. Of these eigenstates, only those without off-diagonal correlations do not decay. Perturbative coupling between the states can be computed by [see also Eq. (S6) in Sec. E]

$$\mathcal{L}_{\text{eff}} = \mathcal{L}_0 - \mathcal{P}\mathcal{L}_1(\mathcal{L}_0)^{-1}\mathcal{L}_1\mathcal{P}\,, \tag{S1}$$

where $\mathcal{P}$ projects into the $\mathcal{L}_0$ eigenstates with zero decay rate.

According to Ref. [37], the transfer rate between sites i and $(i+1)$ depends on the state of the neighboring sites $(i-1)$ and $(i+2)$. Thus, focussing only on the two central spins, the transfer rates can be read from the prefactors of

$$\mathcal{L}_{\text{eff}}^{i,(i+1)} \left|\cdots\uparrow\uparrow\downarrow\uparrow\cdots\right\rangle\left\langle\cdots\uparrow\uparrow\downarrow\uparrow\cdots\right| = \frac{J^2}{4\gamma}\left(\left|\cdots\uparrow\downarrow\uparrow\uparrow\cdots\right\rangle\left\langle\cdots\uparrow\downarrow\uparrow\uparrow\cdots\right| - \left|\cdots\uparrow\uparrow\downarrow\uparrow\cdots\right\rangle\left\langle\cdots\uparrow\uparrow\downarrow\uparrow\cdots\right|\right), \tag{S2}$$

$$\mathcal{L}_{\text{eff}}^{i,(i+1)} \left|\cdots\uparrow\uparrow\downarrow\downarrow\cdots\right\rangle\left\langle\cdots\uparrow\uparrow\downarrow\downarrow\cdots\right| = \frac{J^2\gamma}{4\gamma^2 + J_z^2}\left(\left|\cdots\uparrow\downarrow\uparrow\downarrow\cdots\right\rangle\left\langle\cdots\uparrow\downarrow\uparrow\downarrow\cdots\right| - \left|\cdots\uparrow\uparrow\downarrow\downarrow\cdots\right\rangle\left\langle\cdots\uparrow\uparrow\downarrow\downarrow\cdots\right|\right). \tag{S3}$$

All other possibilities can be obtained by permuting bras and kets, up and down, and reading states from right to left. Here, $\mathcal{L}_{\text{eff}}^{i,(i+1)}$ indicates that only the effective Liouvillian acting on site i and $i+1$ is given, i.e. $\mathcal{L}_{\text{eff}} = \sum_i \mathcal{L}_{\text{eff}}^{i,(i+1)}$.

Since both scenarios are combinatorically equally likely for randomly arranged spins, we compute an effective transfer rate r by taking the *geometric* average, which yields

$$r = \frac{J^2}{2\sqrt{4\gamma^2 + J_z^2}}\,. \tag{S4}$$

From this, we can compute the parameter scaling of S_0 using $S(t) = \log_2(rt)/4 + \mathcal{O}(1) = \log_2(Jt)/4 + \log_2(r/J)/4 + \mathcal{O}(1)$ as

$$S_0 = \frac{1}{4}\log_2\left[\frac{J}{2\sqrt{4\gamma^2 + J_z^2}}\right] + \mathcal{O}(1)\,. \tag{S5}$$

Appendix E: Strong dephasing limits of the Fermi-Hubbard model and of the Bose-Hubbard model

1. Strong dephasing limit of the Fermi-Hubbard model: two decoupled Symmetric Exclusion processes

We define the Fermi-Hubbard Hamiltonian as

$$\hat{H} = -J\sum_{j=1}^{N}[\hat{c}_{\uparrow j+1}^\dagger \hat{c}_{\uparrow j} + \text{h.c.} + \hat{c}_{\downarrow j+1}^\dagger \hat{c}_{\downarrow j} + \text{h.c.}] + U\sum_{j=1}^{N}\hat{c}_{\uparrow j}^\dagger \hat{c}_{\uparrow j}\hat{c}_{\downarrow j}^\dagger \hat{c}_{\downarrow j}, \tag{S1}$$

where $\hat{c}_{\uparrow j}^\dagger$ (resp. $\hat{c}_{\downarrow j}^\dagger$) is the creation operator of a fermion with spin up (resp. down) on site j. We consider the strong dephasing limit of the Lindblad equation

$$\frac{d}{dt}\hat{\rho} = -\mathrm{i}[\hat{H},\hat{\rho}] + \gamma\sum_{j=1}^{N}\mathcal{D}[\hat{c}_{\uparrow j}^\dagger \hat{c}_{\uparrow j}](\hat{\rho}) + \gamma\sum_{j=1}^{N}\mathcal{D}[\hat{c}_{\downarrow j}^\dagger \hat{c}_{\downarrow j}](\hat{\rho}), \tag{S2}$$

where $\mathcal{D}[\hat{A}](\rho) = \hat{A}\hat{\rho}\hat{A}^\dagger - \frac{1}{2}\{\hat{A}^\dagger\hat{A},\hat{\rho}\}$. For our purposes, it is more convenient to write this equation in vectorized form: we vectorize the density matrix $\hat{\rho} \to |\rho\rangle$ —we write the $4^N \times 4^N$ matrix $\hat{\rho}$ as a 4^{2N}-vector $|\rho\rangle$—, and write its evolution as

$$\frac{d}{dt}|\rho\rangle = \gamma\left(\mathcal{L}_0|\rho\rangle + \frac{1}{\gamma}\mathcal{L}_1|\rho\rangle\right) \tag{S3}$$

where $\mathcal{L}_0$ contains the dissipative part of Eq. (S2), and $\mathcal{L}_1$ contains the unitary part in (S2). [Here, contrary to what is done in Ref. [37] and in Sec. D, we do not treat the diagonal and non-diagonal parts of the Hamiltonian differently. Here $\mathcal{L}_1$ corresponds to $-\mathrm{i}[H,\cdot]$ where H is the whole Hamiltonian, including its diagonal part.] Let $\tau = \gamma t$, then

$$\frac{d}{d\tau}|\rho\rangle = \mathcal{L}_0|\rho\rangle + \frac{1}{\gamma}\mathcal{L}_1|\rho\rangle\,, \tag{S4}$$

and the solution of that equation for some arbitrary initial condition $|\rho_0\rangle$ can be expanded to second order in $1/\gamma$,

$$\begin{aligned}|\rho(\tau)\rangle &= \exp\left(\tau\mathcal{L}_0 + \frac{\tau}{\gamma}\mathcal{L}_1\right)|\rho_0\rangle \\ &= e^{\tau\mathcal{L}_0}|\rho_0\rangle + \frac{1}{\gamma}\int_0^\tau d\tau_1 e^{(\tau-\tau_1)\mathcal{L}_0}\mathcal{L}_1 e^{\tau_1\mathcal{L}_0}|\rho_0\rangle \\ &\quad + \frac{1}{\gamma^2}\int_0^\tau d\tau_1\int_0^{\tau_1} d\tau_2 e^{(\tau-\tau_1)\mathcal{L}_0}\mathcal{L}_1 e^{(\tau_1-\tau_2)\mathcal{L}_0}\mathcal{L}_1 e^{\tau_2\mathcal{L}_0}|\rho_0\rangle + \dots\end{aligned} \tag{S5}$$

Importantly, the subspace of density matrices ρ that satisfy $\mathcal{L}_0|\rho\rangle = 0$ is precisely the one of matrices that are diagonal in the computational basis. Let us call $\mathcal{P}$ the projector onto that subspace, and $\mathcal{P}^\perp = 1 - \mathcal{P}$ its orthogonal projector.

Then for $\tau \gg 1$ we can replace $e^{\tau\mathcal{L}_0}$ with $\mathcal{P}$. This leads to

$$\begin{aligned}|\rho(\tau)\rangle &\simeq \mathcal{P}\,|\rho_0\rangle + \frac{\tau}{\gamma}\mathcal{P}\mathcal{L}_1\mathcal{P}\,|\rho_0\rangle + \frac{\tau^2}{2\gamma^2}\mathcal{P}\mathcal{L}_1\mathcal{P}\mathcal{L}_1\mathcal{P}\,|\rho_0\rangle + \frac{1}{\gamma^2}\int_0^\tau d\tau_2(\tau-\tau_2)\mathcal{P}\mathcal{L}_1\mathcal{P}^\perp e^{\tau_2\mathcal{L}_0}\mathcal{P}^\perp\mathcal{L}_1\mathcal{P}\,|\rho_0\rangle + \dots \\ &\simeq \exp\left(\frac{\tau}{\gamma}\mathcal{P}\mathcal{L}_1\mathcal{P}\right)\mathcal{P}\,|\rho_0\rangle + \mathcal{P}\mathcal{L}_1\mathcal{P}^\perp\left(\frac{\tau}{\gamma^2}\int_0^\infty d\tau_2 e^{\tau_2\mathcal{L}_0}\right)\mathcal{P}^\perp\mathcal{L}_1\mathcal{P}\,|\rho_0\rangle + \dots \\ &\simeq \exp\left(\frac{\tau}{\gamma}\mathcal{P}\mathcal{L}_1\mathcal{P}\right)\mathcal{P}\,|\rho_0\rangle + \frac{\tau}{\gamma^2}\mathcal{P}\mathcal{L}_1\mathcal{P}^\perp\left(-\mathcal{L}_0^\perp\right)^{-1}\mathcal{P}^\perp\mathcal{L}_1\mathcal{P}\,|\rho_0\rangle + \dots,\end{aligned}$$

where $\mathcal{L}_0^\perp$ is the restriction of $\mathcal{L}_0$ to the subspace orthogonal to its kernel, and $\left(\mathcal{L}_0^\perp\right)^{-1}$ is its inverse on that subspace. Finally, one notes that $\mathcal{P}\mathcal{L}_1\mathcal{P} = 0$, since $\mathcal{L}_1$ acts on the density matrix ρ as $-i[H,\rho]$. Thus, the result of second-order perturbation theory is that, in the strong dephasing limit, the density matrix remains diagonal on long times scales, $|\rho(t)\rangle \simeq \mathcal{P}\,|\rho(t)\rangle$. The slow evolution of the diagonal part $|\rho_{\text{diag}}(t)\rangle := \mathcal{P}\,|\rho(t)\rangle$ is given by

$$\frac{d}{dt}\,|\rho_{\text{diag}}(t)\rangle \;=\; -\frac{1}{\gamma}\mathcal{P}\mathcal{L}_1\mathcal{P}^\perp\left(\mathcal{L}_0^\perp\right)^{-1}\mathcal{P}^\perp\mathcal{L}_1\mathcal{P}\,|\rho_{\text{diag}}(t)\rangle\,. \tag{S6}$$

This equation has been obtained for the XXZ chain by Cai and Barthel [37] and also for other models, including models of bosons, by Bernard, Jin and Shpielberg [63]. Let us now apply it to the Fermi-Hubbard model (S1). The key observation is that the interacting term $U\sum_{j=1}^N \hat{c}^\dagger_{\uparrow j}\hat{c}_{\uparrow j}\hat{c}^\dagger_{\downarrow j}\hat{c}_{\downarrow j}$ in the Hamiltonian (S1) acts diagonally in the computational basis, so it does not contribute to the term $-\frac{1}{\gamma}\mathcal{P}\mathcal{L}_1\mathcal{P}^\perp\left(\mathcal{L}_0^\perp\right)^{-1}\mathcal{P}^\perp\mathcal{L}_1\mathcal{P}$ in Eq. (S6). Therefore, in the strong dephasing limit, the spin components $\uparrow$ and $\downarrow$ simply decouple, and each spin component follows its own strong-dephasing dynamics. One can then simply set $U = 0$ in the Hamiltonian (S1) which splits into two independent models of non-interacting fermions, one for each spin component. Consequently, the strong-dephasing limit of the Fermi-Hubbard model consists of two decoupled Symmetric Exclusion Processes, one for the spins $\uparrow$, the other for the spins $\downarrow$, as claimed in the main text.

2. Strong dephasing limit of the Bose-Hubbard model: a Symmetric 'Inclusion' Process

We define the Bose-Hubbard Hamiltonian as

$$\hat{H} = -J\sum_{j=1}^N[\hat{b}^\dagger_{j+1}\hat{b}_j + \text{h.c.}] + \frac{U}{2}\sum_{j=1}^N \hat{b}^\dagger_j\hat{b}_j(\hat{b}^\dagger_j\hat{b}_j - 1) \tag{S7}$$

and the Lindlblad equation with dephasing takes the form (see e.g. Ref. [47])

$$\frac{d}{dt}\rho = -\mathrm{i}[\hat{H},\hat{\rho}] + \gamma\sum_{j=1}^N \mathcal{D}[\hat{b}^\dagger_j\hat{b}_j](\hat{\rho}). \tag{S8}$$

Like for the XXZ chain and for the Fermi-Hubbard model, the strong dephasing limit can be analyzed in second-order perturbation theory [37, 63]. The general formula (S6), where $\gamma\mathcal{L}_0$ is the dissipative part of the Lindblad equation and $\mathcal{L}_1$ is the unitary part, applies also to the Bose-Hubbard model. As in the Fermi-Hubbard case, the interaction term $\frac{U}{2}\sum_{j=1}^N \hat{b}^\dagger_j\hat{b}_j(\hat{b}^\dagger_j\hat{b}_j - 1)$ in the Hamiltonian (S7) acts diagonally in the single-site Fock basis. Consequently, it does not contribute to the term $-\frac{1}{\gamma}\mathcal{P}\mathcal{L}_1\mathcal{P}^\perp\left(\mathcal{L}_0^\perp\right)^{-1}\mathcal{P}^\perp\mathcal{L}_1\mathcal{P}$. At strong dephasing the Hubbard interaction is irrelevant, and the model can be analyzed simply by setting $U = 0$. The resulting model of non-interacting bosons with dephasing has been analyzed in Ref. [63]. For the convenience of the reader, here we briefly sketch a simple derivation of that strong-dephasing limit.

For notational simplicity, we focus on $N = 2$ two sites only, and label the basis states as $|n_1 n_2\rangle$ where $n_1, n_2 \in \mathbb{N}$ are the number of bosons on site 1 and 2. Diagonal density matrices are of the form

$$\rho_{\text{diag}} = \sum_{n_1,n_2} p(n_1,n_2)\,|n_1 n_2\rangle\,\langle n_1 n_2|\,. \tag{S9}$$

Under strong dephasing, the effective dynamics within the space of diagonal density matrices must be a classical stochastic process for the probability distribution $p(n_1,n_2)$. The goal is to determine the rates that define the classical master equation of that process.

We proceed step by step to compute the r.h.s of Eq. (S6). First, $\mathcal{L}_1\mathcal{P}\left|\rho_{\rm diag}\right\rangle = \mathcal{L}_1\left|\rho_{\rm diag}\right\rangle$ is the vectorized form of

$$\begin{aligned}
-\mathrm{i}\left[\hat{H},\rho_{\rm diag}\right] &= -\mathrm{i}\left[H,\sum_{n_1,n_2} p(n_1,n_2)\left|n_1n_2\right\rangle\left\langle n_1n_2\right|\right] \\
&= \mathrm{i}J\sum_{n_1,n_2} p(n_1,n_2)\Big(\sqrt{(n_1+1)n_2}\left|n_1+1,n_2-1\right\rangle\left\langle n_1n_2\right| + \sqrt{n_1(n_2+1)}\left|n_1-1,n_2+1\right\rangle\left\langle n_1n_2\right| \\
&\quad - \sqrt{(n_1+1)n_2}\left|n_1,n_2\right\rangle\left\langle n_1+1n_2-1\right| + \sqrt{n_1(n_2+1)}\left|n_1,n_2\right\rangle\left\langle n_1-1,n_2+1\right|\Big),
\end{aligned}$$

which we write as

$$\begin{aligned}
\mathcal{L}_1\left|\rho_{\rm diag}\right\rangle = \mathrm{i}J\sum_{n_1,n_2} p(n_1,n_2)\Big(&\sqrt{(n_1+1)n_2}\left|n_1+1,n_2-1\right\rangle\left\langle n_1n_2\right| + \sqrt{n_1(n_2+1)}\left|n_1-1,n_2+1\right\rangle\left|n_1n_2\right\rangle \\
&- \sqrt{(n_1+1)n_2}\left|n_1,n_2\right\rangle\left\langle n_1+1n_2-1\right| + \sqrt{n_1(n_2+1)}\left|n_1,n_2\right\rangle\left|n_1-1,n_2+1\right\rangle\Big).
\end{aligned}$$

Second, we observe that $\mathcal{L}[\hat{b}_1^\dagger\hat{b}_1]\left|n_1\pm1,n_2'\right\rangle\left|n_1,n_2\right\rangle = (n_1\pm1)n_1 - \frac{(n_1\pm1)^2+n_1^2}{2} = -\frac{1}{2}$. Then

$$\begin{aligned}
(\mathcal{L}_0^\perp)^{-1}\mathcal{P}^\perp\mathcal{L}_1\mathcal{P}\left|\rho_{\rm diag}\right\rangle = \frac{-iJ}{2\gamma}\sum_{n_1,n_2} p(n_1,n_2)\Big(&\sqrt{(n_1+1)n_2}\left|n_1+1,n_2-1\right\rangle\left|n_1n_2\right\rangle + \sqrt{n_1(n_2+1)}\left|n_1-1,n_2+1\right\rangle\left|n_1n_2\right\rangle \\
&- \sqrt{(n_1+1)n_2}\left|n_1,n_2\right\rangle\left|n_1+1n_2-1\right\rangle + \sqrt{n_1(n_2+1)}\left|n_1,n_2\right\rangle\left|n_1-1,n_2+1\right\rangle\Big).
\end{aligned}$$

Applying again the vectorized form of $-\mathrm{i}[\hat{H},.]$, and projecting onto diagonal configurations, one arrives at

$$\begin{aligned}
-\mathcal{P}\mathcal{L}_1\mathcal{P}^\perp(\mathcal{L}_0^\perp)^{-1}\mathcal{P}^\perp\mathcal{L}_1\mathcal{P}\left|\rho_{\rm diag}\right\rangle = \frac{J^2}{2\gamma}\sum_{n_1,n_2} p(n_1,n_2)& \\
\Big(\sqrt{(n_1+1)n_2}^2(\left|n_1+1,n_2-1\right\rangle\left|n_1+1n_2-1\right\rangle - \left|n_1,n_2\right\rangle\left|n_1n_2\right\rangle)& \\
+\sqrt{n_1(n_2+1)}^2(\left|n_1-1,n_2+1\right\rangle\left|n_1-1n_2+1\right\rangle - \left|n_1,n_2\right\rangle\left|n_1n_2\right\rangle)& \\
+\sqrt{(n_1+1)n_2}^2(\left|n_1+1,n_2-1\right\rangle\left|n_1+1n_2-1\right\rangle - \left|n_1,n_2\right\rangle\left|n_1n_2\right\rangle)& \\
+\sqrt{n_1(n_2+1)}^2(\left|n_1-1,n_2+1\right\rangle\left|n_1-1,n_2+1\right\rangle - \left|n_1,n_2\right\rangle\left|n_1,n_2\right\rangle)\Big)&.
\end{aligned}$$

In conclusion, the classical master equation obeyed by the probability distribution $p(n_1,n_2)$ is

$$\begin{aligned}
\frac{d}{dt}p(n_1,n_2) = \frac{J^2}{\gamma}n_1(n_2+1)[p(n_1-1,n_2+1)-p(n_1,n_2)] \\
+\frac{J^2}{\gamma}(n_1+1)n_2[p(n_1+1,n_2-1)-p(n_1,n_2)].
\end{aligned} \tag{S10}$$

This result generalizes straightforwardly to the case with more sites, $N>2$, i.e.

$$\begin{aligned}
\frac{d}{dt}p(n_1,n_2,\dots,n_N) = \frac{J^2}{\gamma}\sum_i n_i[(n_{i-1}+1)p(\dots,n_{i-1}+1,n_i-1,\dots)+(n_{i+1}+1)p(\dots,n_i-1,n_{i+1}+1,\dots) \\
-(n_{i-1}+n_{i+1}+2)p(\dots,n_i,n_{i+1},\dots)].
\end{aligned} \tag{S11}$$

What is interesting about the master equation (S11) is that it is very different from the one of non-interacting particles undergoing a random walk, which would rather be of the form

$$\frac{d}{dt}p(n_1,n_2,\dots,n_N) \propto \sum_i n_i[p(\dots,n_i-1,n_{i+1}+1,\dots)+p(\dots,n_{i-1}+1,n_i-1,\dots)-2p(\dots,n_{i-1},n_i,n_{i+1},\dots)].$$

Interestingly, the resulting classical dynamics exhibits a signature of bosonic bunching in the original quantum model. The classical stochastic process defined by Eq. (S11) belongs to a class of models known as 'Symmetric Inclusion Processes' in the statistical physics literature, see e.g. Refs. [88, 89].

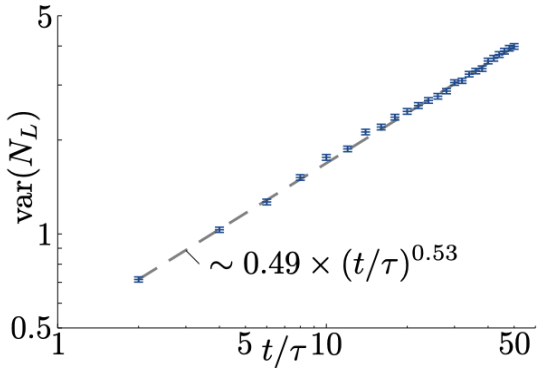

FIG. S4. Fit for the variance growth for the Symmetric Inclusion Process. The blue crosses are determined by a Monte Carlo simulation of Eq. (S11) with 5000 trajectories. The grey dashed line is a power law fit to the numerical data.

In order to determine the dynamics of number fluctuations in the model described by Eq. (S11), we numerically compute $n_{\text{samples}} = 5000$ different sample trajectories for a chain of length $L = 100$. Fig. S4 shows the time trace of the variance of the number of particles in the left half of the chain $\text{var}(N_L)$ [corrected by $n_{\text{samples}}/(n_{\text{samples}} - 1)$]. We compute the error of the variance using the jackknife method [90] by separating the data into $M = 500$ bins with 10 trajectories each. Then, we compute the variances v_m for all possible subsets of $M - 1$ different bins (i.e. deleting 1 bin for each subset). Finally, we compute the error from these variances as

$$\text{error}[\text{var}(N_L)] = \sqrt{\frac{M-1}{M} \sum_m \left[v_m - \text{var}(N_L)\right]^2}\,. \tag{S12}$$

We use `LsqFit.jl` to fit the numerical data with a power law of the form $\text{var}(N_L) = a \times (t/\tau)^b$, and find $a \approx 0.49$ and $b = 0.53$, close to $b = 1/2$. We find that this fit describes the data well, as shown in Fig. S4. Here, $\tau = \gamma/J^2$ is the characteristic time scale of the dynamics.

If we thus assume that N_L is Gaussian distributed with standard deviation $\delta \sim (t/\tau)^{b/2}$, we can use Eq. (7) of the main text to compute $S_{\text{num}}(t) = \log_2[(t/\tau)^{b/2}] + \mathcal{O}(1)$, close to $\log_2(t/\tau)/4 + \text{const.}$ used in the main text.

* schachenmayer@unistra.fr

[1] L. Amico, R. Fazio, A. Osterloh, and V. Vedral, Entanglement in many-body systems, Rev. Mod. Phys. **80**, 517 (2008).

[2] J. Eisert, M. Cramer, and M. B. Plenio, Colloquium: Area laws for the entanglement entropy, Rev. Mod. Phys. **82**, 277 (2010).

[3] P. Calabrese and J. Cardy, Evolution of entanglement entropy in one-dimensional systems, J. Stat. Mech.: Theory Exp. **2005** (04), P04010.

[4] M. Fagotti and P. Calabrese, Evolution of entanglement entropy following a quantum quench: Analytic results for the xy chain in a transverse magnetic field, Phys. Rev. A **78**, 010306(R) (2008).

[5] M. Žnidarič, T. Prosen, and P. Prelovšek, Many-body localization in the Heisenberg XXZ magnet in a random field, Phys. Rev. B **77**, 064426 (2008).

[6] V. Alba and P. Calabrese, Entanglement and thermodynamics after a quantum quench in integrable systems, Proc. Natl. Acad. Sci. U. S. A. **114**, 7947 (2017).

[7] C. Jonay, D. A. Huse, and A. Nahum, Coarse-grained dynamics of operator and state entanglement, arXiv:1803.00089 (2018).

[8] A. Lukin, M. Rispoli, R. Schittko, M. E. Tai, A. M. Kaufman, S. Choi, V. Khemani, J. Léonard, and M. Greiner, Probing entanglement in a many-body–localized system, Science **364**, 256 (2019).

[9] G. Vidal, Efficient Simulation of One-Dimensional Quantum Many-Body Systems, Phys. Rev. Lett. **93**, 040502 (2004).

[10] F. Verstraete, V. Murg, and J. I. Cirac, Matrix product states, projected entangled pair states, and variational renormalization group methods for quantum spin systems, Adv. Phys. **57**, 143 (2008).

[11] U. Schollwöck, The density-matrix renormalization group in the age of matrix product states, Ann. Phys. **326**, 96 (2011).

[12] S. Paeckel, T. Köhler, A. Swoboda, S. R. Manmana, U. Schollwöck, and C. Hubig, Time-evolution methods for matrix-product states, Ann. Phys. **411**, 167998 (2019).

[13] N. Schuch, M. M. Wolf, F. Verstraete, and J. I. Cirac, Entropy Scaling and Simulability by Matrix Product States, Phys. Rev. Lett. **100**, 030504 (2008).

[14] I. Bloch, J. Dalibard, and S. Nascimbène, Quantum simulations with ultracold quantum gases, Nat. Phys. **8**, 267 (2012).

[15] C. S. Adams, J. D. Pritchard, and J. P. Shaffer, Rydberg atom quantum technologies, J. Phys. B: At. Mol. Opt.

Phys. **53**, 012002 (2019).
[16] A. Browaeys and T. Lahaye, Many-body physics with individually controlled Rydberg atoms, Nat. Phys. **16**, 132 (2020).
[17] M. Morgado and S. Whitlock, Quantum simulation and computing with Rydberg-interacting qubits, AVS Quantum Sci. **3**, 023501 (2021).
[18] B. Gadway and B. Yan, Strongly interacting ultracold polar molecules, J. Phys. B: At. Mol. Opt. Phys. **49**, 152002 (2016).
[19] R. Blatt and C. F. Roos, Quantum simulations with trapped ions, Nat. Phys. **8**, 277 (2012).
[20] J. I. Cirac and P. Zoller, Goals and opportunities in quantum simulation, Nat. Phys. **8**, 264 (2012).
[21] I. M. Georgescu, S. Ashhab, and F. Nori, Quantum simulation, Rev. Mod. Phys. **86**, 153 (2014).
[22] P. Zanardi, C. Zalka, and L. Faoro, Entangling power of quantum evolutions, Phys. Rev. A **62**, 030301(R) (2000).
[23] P. Zanardi, Entanglement of quantum evolutions, Phys. Rev. A **63**, 040304(R) (2001).
[24] X. Wang and P. Zanardi, Quantum entanglement of unitary operators on bipartite systems, Phys. Rev. A **66**, 044303 (2002).
[25] T. Prosen and I. Pižorn, Operator space entanglement entropy in a transverse Ising chain, Phys. Rev. A **76**, 032316 (2007).
[26] J. Dubail, Entanglement scaling of operators: a conformal field theory approach, with a glimpse of simulability of long-time dynamics in 1+1d, Journal of Physics A: Mathematical and Theoretical **50**, 234001 (2017).
[27] T. Zhou and D. J. Luitz, Operator entanglement entropy of the time evolution operator in chaotic systems, Phys. Rev. B **95**, 094206 (2017).
[28] V. Alba, J. Dubail, and M. Medenjak, Operator entanglement in interacting integrable quantum systems: The case of the rule 54 chain, Phys. Rev. Lett. **122**, 250603 (2019).
[29] H. Wang and T. Zhou, Barrier from chaos: operator entanglement dynamics of the reduced density matrix, J. High Energy Phys. **2019** (12), 1.
[30] G. Styliaris, N. Anand, and P. Zanardi, Information Scrambling over Bipartitions: Equilibration, Entropy Production, and Typicality, Phys. Rev. Lett. **126**, 030601 (2021).
[31] Note that here this indicates approximability w.r.t. the two-norm of the vectorized density matrix.
[32] K. Noh, L. Jiang, and B. Fefferman, Efficient classical simulation of noisy random quantum circuits in one dimension, Quantum **4**, 318 (2020), 2003.13163v3.
[33] T. Rakovszky, C. W. von Keyserlingk, and F. Pollmann, Dissipation-assisted operator evolution method for capturing hydrodynamic transport, arXiv:2004.05177 (2020).
[34] B. Bertini, P. Kos, and T. Prosen, Operator Entanglement in Local Quantum Circuits I: Chaotic Dual-Unitary Circuits, SciPost Phys. **8**, 067 (2020).
[35] B. Bertini, P. Kos, and T. Prosen, Operator Entanglement in Local Quantum Circuits II: Solitons in Chains of Qubits, SciPost Phys. **8**, 068 (2020).
[36] D. Rossini and E. Vicari, Coherent and dissipative dynamics at quantum phase transitions, Physics Reports **936**, 1 (2021).
[37] Z. Cai and T. Barthel, Algebraic versus Exponential Decoherence in Dissipative Many-Particle Systems, Phys. Rev. Lett. **111**, 150403 (2013).
[38] M. V. Medvedyeva, F. H. L. Essler, and T. Prosen, Exact Bethe Ansatz Spectrum of a Tight-Binding Chain with Dephasing Noise, Phys. Rev. Lett. **117**, 137202 (2016).
[39] M. Foss-Feig, J. T. Young, V. V. Albert, A. V. Gorshkov, and M. F. Maghrebi, Solvable Family of Driven-Dissipative Many-Body Systems, Phys. Rev. Lett. **119**, 190402 (2017).
[40] M. Žnidarič, Relaxation times of dissipative many-body quantum systems, Phys. Rev. E **92**, 042143 (2015).
[41] D. Poletti, J.-S. Bernier, A. Georges, and C. Kollath, Interaction-Induced Impeding of Decoherence and Anomalous Diffusion, Phys. Rev. Lett. **109**, 045302 (2012).
[42] D. Poletti, P. Barmettler, A. Georges, and C. Kollath, Emergence of Glasslike Dynamics for Dissipative and Strongly Interacting Bosons, Phys. Rev. Lett. **111**, 195301 (2013).
[43] J. Ren, Q. Li, W. Li, Z. Cai, and X. Wang, Noise-Driven Universal Dynamics towards an Infinite Temperature State, Phys. Rev. Lett. **124**, 130602 (2020).
[44] R. Bouganne, M. Bosch Aguilera, A. Ghermaoui, J. Beugnon, and F. Gerbier, Anomalous decay of coherence in a dissipative many-body system, Nat. Phys. **16**, 21 (2020).
[45] D. Plankensteiner, J. Schachenmayer, H. Ritsch, and C. Genes, Laser noise imposed limitations of ensemble quantum metrology, J. Phys. B: At. Mol. Opt. Phys. **49**, 245501 (2016).
[46] C. W. Gardiner and P. Zoller, *Quantum noise* (Springer, 1991) Chap. 3.6, p. 77.
[47] H. Pichler, A. J. Daley, and P. Zoller, Nonequilibrium dynamics of bosonic atoms in optical lattices: Decoherence of many-body states due to spontaneous emission, Phys. Rev. A **82**, 063605 (2010).
[48] R. Orús and G. Vidal, Infinite time-evolving block decimation algorithm beyond unitary evolution, Phys. Rev. B **78**, 155117 (2008).
[49] T. E. Harris, Diffusion with "Collisions" between Particles, J. Appl. Probab. **2**, 323 (1965).
[50] D. G. Levitt, Dynamics of a Single-File Pore: Non-Fickian Behavior, Phys. Rev. A **8**, 3050 (1973).
[51] R. Arratia, The Motion of a Tagged Particle in the Simple Symmetric Exclusion System on Z, aop **11**, 362 (1983).
[52] H. Weimer, A. Kshetrimayum, and R. Orús, Simulation methods for open quantum many-body systems, Rev. Mod. Phys. **93**, 015008 (2021).
[53] A. J. Daley, Quantum trajectories and open many-body quantum systems, Adv. Phys. **63**, 77 (2014).
[54] M. Zwolak and G. Vidal, Mixed-State Dynamics in One-Dimensional Quantum Lattice Systems: A Time-Dependent Superoperator Renormalization Algorithm, Phys. Rev. Lett. **93**, 207205 (2004).
[55] F. Verstraete, J. J. García-Ripoll, and J. I. Cirac, Matrix Product Density Operators: Simulation of Finite-Temperature and Dissipative Systems, Phys. Rev. Lett. **93**, 207204 (2004).
[56] A. H. Werner, D. Jaschke, P. Silvi, M. Kliesch, T. Calarco, J. Eisert, and S. Montangero, Positive Tensor Network Approach for Simulating Open Quantum Many-Body Systems, Phys. Rev. Lett. **116**, 237201 (2016).
[57] G. Vidal, Classical Simulation of Infinite-Size Quantum Lattice Systems in One Spatial Dimension, Phys. Rev. Lett. **98**, 070201 (2007).

[58] A. T. Sornborger and E. D. Stewart, Higher-order methods for simulations on quantum computers, Phys. Rev. A **60**, 1956 (1999).

[59] F. Carollo and V. Alba, Emergent dissipative quasiparticle picture in noninteracting Markovian open quantum systems, arXiv:2106.11997 (2021).

[60] V. Alba and F. Carollo, Hydrodynamics of quantum entropies in Ising chains with linear dissipation, arXiv:2109.01836 (2021).

[61] M. V. Medvedyeva, T. Prosen, and M. Žnidarič, Influence of dephasing on many-body localization, Phys. Rev. B **93**, 094205 (2016).

[62] K. Mallick, The exclusion process: A paradigm for non-equilibrium behaviour, Physica A **418**, 17 (2015).

[63] D. Bernard, T. Jin, and O. Shpielberg, Transport in quantum chains under strong monitoring, EPL (Europhysics Letters) **121**, 60006 (2018).

[64] B. Lin, M. Meron, B. Cui, S. A. Rice, and H. Diamant, From Random Walk to Single-File Diffusion, Phys. Rev. Lett. **94**, 216001 (2005).

[65] B. Derrida and A. Gerschenfeld, Current Fluctuations of the One Dimensional Symmetric Simple Exclusion Process with Step Initial Condition, J. Stat. Phys. **136**, 1 (2009).

[66] T. Imamura, K. Mallick, and T. Sasamoto, Large Deviations of a Tracer in the Symmetric Exclusion Process, Phys. Rev. Lett. **118**, 160601 (2017).

[67] A. Grabsch, A. Poncet, P. Rizkallah, P. Illien, and O. Bénichou, Closing and solving the hierarchy for large deviations and spatial correlations in single-file diffusion, arXiv:2110.09269 (2021).

[68] K. Hahn, J. Kärger, and V. Kukla, Single-File Diffusion Observation, Phys. Rev. Lett. **76**, 2762 (1996).

[69] Q.-H. Wei, C. Bechinger, and P. Leiderer, Single-File Diffusion of Colloids in One-Dimensional Channels, Science **287**, 625 (2000).

[70] M. Žnidarič, Dephasing-induced diffusive transport in the anisotropic Heisenberg model, New J. Phys. **12**, 043001 (2010).

[71] M. Žnidarič, Exact solution for a diffusive nonequilibrium steady state of an open quantum, J. Stat. Mech.: Theory Exp. **2010** (05), L05002.

[72] V. Eisler, Crossover between ballistic and diffusive transport: the quantum exclusion process, J. Stat. Mech.: Theory Exp. **2011** (06), P06007.

[73] J. De Nardis, S. Gopalakrishnan, R. Vasseur, and B. Ware, Subdiffusive hydrodynamics of nearly-integrable anisotropic spin chains, arXiv:2109.13251 (2021).

[74] M. Goldstein and E. Sela, Symmetry-resolved entanglement in many-body systems, Phys. Rev. Lett. **120**, 200602 (2018).

[75] J. C. Xavier, F. C. Alcaraz, and G. Sierra, Equipartition of the entanglement entropy, Phys. Rev. B **98**, 041106(R) (2018).

[76] G. Parez, R. Bonsignori, and P. Calabrese, Quasiparticle dynamics of symmetry-resolved entanglement after a quench: Examples of conformal field theories and free fermions, Phys. Rev. B **103**, L041104 (2021).

[77] H. Barghathi, C. M. Herdman, and A. Del Maestro, Rényi Generalization of the Accessible Entanglement Entropy, Phys. Rev. Lett. **121**, 150501 (2018).

[78] H. Barghathi, E. Casiano-Diaz, and A. Del Maestro, Operationally accessible entanglement of one-dimensional spinless fermions, Phys. Rev. A **100**, 022324 (2019).

[79] Y. Li, X. Chen, and M. P. A. Fisher, Quantum Zeno effect and the many-body entanglement transition, Phys. Rev. B **98**, 205136 (2018).

[80] A. Chan, R. M. Nandkishore, M. Pretko, and G. Smith, Unitary-projective entanglement dynamics, Phys. Rev. B **99**, 224307 (2019).

[81] M. Coppola, E. Tirrito, D. Karevski, and M. Collura, Growth of entanglement entropy under local projective measurements, arXiv:2109.10837 (2021).

[82] T. Botzung, S. Diehl, and M. Müller, Engineered dissipation induced entanglement transition in quantum spin chains: From logarithmic growth to area law, Phys. Rev. B **104**, 184422 (2021).

[83] M. J. Mark, S. Flannigan, F. Meinert, J. P. D'Incao, A. J. Daley, and H.-C. Nägerl, Interplay between coherent and dissipative dynamics of bosonic doublons in an optical lattice, Phys. Rev. Res. **2**, 043050 (2020).

[84] B. Zhu, B. Gadway, M. Foss-Feig, J. Schachenmayer, M. L. Wall, K. R. A. Hazzard, B. Yan, S. A. Moses, J. P. Covey, D. S. Jin, J. Ye, M. Holland, and A. M. Rey, Suppressing the Loss of Ultracold Molecules Via the Continuous Quantum Zeno Effect, Phys. Rev. Lett. **112**, 070404 (2014).

[85] V. S. Shchesnovich and V. V. Konotop, Control of a Bose-Einstein condensate by dissipation: Nonlinear Zeno effect, Phys. Rev. A **81**, 053611 (2010).

[86] T. Müller, S. Diehl, and M. Buchhold, Measurement-Induced Dark State Phase Transitions in Long-Ranged Fermion Systems, Phys. Rev. Lett. **128**, 010605 (2022).

[87] M. Fishman, S. R. White, and E. M. Stoudenmire, The ITensor software library for tensor network calculations, arXiv:2007.14822 (2020).

[88] C. Giardina, F. Redig, and K. Vafayi, Correlation inequalities for interacting particle systems with duality, Journal of Statistical Physics **141**, 242 (2010).

[89] S. Grosskinsky, F. Redig, and K. Vafayi, Dynamics of condensation in the symmetric inclusion process, Electronic Journal of Probability **18**, 1 (2013).

[90] R. G. Miller, The jackknife-a review, Biometrika **61**, 1 (1974).